Extraction of Micro-Doppler Frequency From HRRPs of Rotating Targets

**XIAO-YI PAN[1], JIAQI LIU[2], LE-TAO XU[1], (Student Member, IEEE), XIA AI[2],
QIANPENG XIE[3], BO YU[4], AND CHENG LI[5]**
[1]State Key Laboratory of Complex Electromagnetic Environment Effects on Electronics and Information System, National University of Defense Technology, Changsha 410073, China
[2]National Key Laboratory of Science and Technology on Test Physics & Numerical Mathematics, Beijing 100000, China
[3]College of Electronic Science and Engineering, National University of Defense Technology, Changsha 410073, China
[4]School of Computer, National University of Defense Technology, Changsha 410073, China
[5]Nanjing Telecommunication Technology Research Institute, Nanjing, China

Corresponding author: Xiao-Yi Pan (pan_xiao_yi@hotmail.com)

ABSTRACT Micro-motion dynamics, such as rapid rotation, vibration and spinning motion, impose additional time-varying frequency modulation on the returned radar signals, which is known as the micro-Doppler (m-D) effect. Micro-Doppler frequency is considered as a stable and unique feature, where the uniqueness means that different micro-motions have distinct signatures. Thus, radar m-D feature extraction is of great potential in target classification and identification. This paper presents m-D frequency estimation from the HRRPs of rotating targets in frequency-stepped signal (FSS) based on the circular correlation (CC) coefficients and the circular average magnitude difference (CAMD) coefficients. The m-D frequency of rotating targets can be estimated accurately from the two proposed methods and the corresponding computational cost burden is also investigated. The accuracy and efficiency of the estimations are compared and revealed by the simulated trials and experimental data.

INDEX TERMS Rotating targets, high resolution range profiles (HRRPs), frequency-stepped signal (FSS), feature extraction, circular correlation (CC) coefficients, circular average magnitude difference (CAMD) coefficients.

I. INTRODUCTION

In addition to the bulk motions, radar targets or any structures on the targets may incorporate rapidly periodic micro-motion dynamics, such as spinning ballistic targets, swing arms and legs of human beings and rotating rotor blades of helicopters, which impose additional time-varying frequency modulation on the returned radar signals [1]–[5]. This modulation is known as micro-Doppler (m-D) effect and the modulation period in frequency is denoted as m-D modulation frequency, i.e., m-D frequency, which provides significant information of the micro-motion dynamics [6]–[10]. Thus, as a stable and unique feature, m-D frequency can be used to distinguish targets or components with various motions. For example, ballistic missiles can be discriminated from the other nearby ballistic targets (such as boosters, decoys and debris) since the intrinsic nutation motion of war-heads induces distinct m-D features [8]. The feature extraction for automatic target recognition (ATR) have received increasing attention among the

radar community [4], [11]–[13]. Traditional time-frequency-based (TF-based) feature extraction techniques rely primarily on the assumption that more than one oscillation of the sinusoidal frequency modulation (FM) curves of high resolution m-D frequency can be achieved [5], [10]. High frequency resolution needs not only a long dwell time but also a high-resolution TF transform which may increase the observation time and the computational complexity [14]. Usually, bilinear transforms, such as the Wigner–Ville distribution (WVD), has better joint time–frequency resolution than any linear transform, such as the short-time Fourier transform (STFT) [15]. Since the radar signal is frequently a multi-component signal, regarding the interference, the cross term of bilinear transforms (such as the WVD) may be unavoidable in the TF plane. Thus, more sophisticated improved TF distribution is addressed to reduce the cross-term interference (such as the smoothed pseudo Wigner-Ville distribution, SPWVD). Especially due to the shield effect,

the m-D curves in the TF plane may be only partial at certain aspect angles [16]. Based on the above factors, conventional feature extraction methods based on the m-D curves in the TF plane may not be effective [5], [17], [18], [21], [23], and this deficiency is what motivates this paper.

Large time-bandwidth product signals are frequently adopted to synthesize high resolution range profiles (HRRPs), such as the chirp signals, the frequency-stepped signals (FSS) and the frequency-stepped chirp signals (FSCS) [5], [19], [20]. HRRPs can also be utilized in feature extraction of targets with micro-motion dynamics [5], [21]–[23]. The main advantage of FSS, compared with other kinds of high resolution radar signals, is that it can easily achieve high range resolution without expensive hardware to support the instantaneous wide bandwidth [5]. For a wideband target recognition radar with FSS, HRRPs can be easily reconstructed by one dimensional (1-D) inverse fast Fourier transform (IFFT) while the m-D curves in TF imaging plane should be achieved by TF-based algorithm which is more time-consuming [14], [24]. Especially in a case of multiple targets with close velocity, m-D signatures will be non-separable in TF plane and HRRP based method may be a better choice if targets can be separated by range [12], [25]. Moreover, conventional m-D parameter estimation methods, such as Hough Transform (HT) and extended Hough Transform (EHT), are not only time-consuming but also easily run into local optimums when the dimension of parameters increases [18], [26]. The features of rotating targets with two symmetrical corner reflectors are extracted from HRRPs via FSS based on the three-point model. However, the three-point model is derived under the assumption that the curves of HRRPs are sinusoidal which would be disturbed in the case of rotating targets with translation motion. In view of this, the m-D frequency of rapid rotating targets is extracted from the reconstructed HRRPs via FSS based on the circular correlation (CC) coefficients and the circular average magnitude difference (CAMD) coefficients in this paper. The reconstructed HRRPs of rapidly periodic rotating targets moving at constant speed in the slow-time-range plane are presented and the circular periodicity of HRRPs is also revealed. The CC coefficients and CAMD coefficients are then employed to characterize the circular periodicity of HRRPs and to provide estimates of the rotating frequency, respectively. The advantage of the proposed methods in this paper is that feature extraction based on the CC and CAMD coefficients can deal with rotating targets with or without a translation velocity benefiting from the circular periodicity of HRRPs while the method mentioned in reference [5] is only suitable for rotating targets with no translation motion.

The rest of the paper is organized as follows: The reconstructions of HRRPs of rapidly periodic rotating targets with a constant speed in FSS radar system are depicted in Section II. In Section III, the circular periodicity of the reconstructed HRRPs is uncovered and the rotating frequency is estimated via the CC coefficients and CAMD coefficients. Experiments with simulated and real data reveal the accuracy and the efficiency of the proposed feature extraction algorithms in Section IV and Section V. Concluding remarks are provided in Section VI.

II. MODELING OF RECONSTRUCTED HRRPS

Targets or components on targets with rapidly periodic rotation are common in rotating rotor blades, scanning antennas, turbines, etc. In this section, HRRPs of rapidly periodic rotating targets moving at constant speed in FSS are first addressed. Then the circular periodicity of HRRPs is depicted.
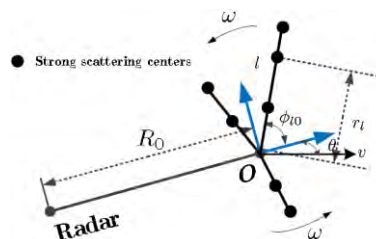

FIGURE 1. Geometry of the rapid rotating targets moving at constant speed in FSS radar.

Figure.1 shows the geometry of the radar and the rotating target with L strong scattering centers in a translation velocity v. The target rotates along the point O which is chosen as the origin and XOY is constructed as the body-fixed coordinate system with X axis paralleling with the line of sight (LOS). The angle between LOS and the translation motion direction is denoted as θ. The rotating velocity is denoted as $\omega = 2\pi f_d$, where f_d is m-D frequency, i.e. rotating frequency, and $T_d = 1/f_d$ is m-D modulation period. Usually, the rotating targets model in Figure 1 can cover most of the typical scenarios in practice. For example, the two-blade rotors are just the case that there are only two rotating blades with radius of equal length and symmetrical about the origin O, while the three-blade rotors are the case that there are three rotating blades with radius of equal length and separated by 120 degrees. And the scattering centers of each blade can be determined by the physical optics (PO) facet prediction model [27]. However, in the scattering at high frequencies, the radar echoes from the rotating target can be approximated as the sum of scattering from a finite number of individual point-scatterers (namely scattering centers) and the scattering center model has already been proven to be good enough in radar signal simulation [28], [29].

Without loss of generality, suppose that there are strong scattering centers on the moving target together. Consider the l-th ($l \in [1, L]$) scattering center and the rotating radius is denoted as r_l. At time $t = 0$, the distance from the radar to the origin O is denoted by R_0 and the initial distance from the radar to the scattering center l can be calculated as $R_{l0} = \sqrt{R_0^2 + r_l^2 + 2R_0 r_l \cos \phi_{l0}}$ where ϕ_{l0} is the initial rotation angle. Then at time the range of the scattering center l measured from the radar can be expressed by

$$R_{lt} = R_{l0} + vt \cos \theta - r_l \cos (\omega t + \phi_{l0}) \qquad (1)$$

The FSS uses a sequence of narrow sub-pulses to achieve wide bandwidth, where each sub-pulse has a single carrier frequency f_0 changing by a fixed amount Δf. The received baseband signal returned form the scatterering center l follows

$$s_{lt} = \sigma_l \text{rect}\left(\frac{t - \frac{2R_{lt}}{c}}{T_P}\right) \cdot \exp\left(\frac{-j4\pi f_n R_{lt}}{c}\right) \quad (2)$$

where σ_l is the backscattering coefficient of l; $rect\,(\cdot)$ is a rectangular window; T_p is pulse width; c is the wave propagation velocity; $n = 0, 1, 2, \ldots, N-1$ denotes the n-th sub-pulse in a burst and $f_n = f_0 + n\Delta f$ denotes the corresponding carrier frequency.

It has been proven that the phase of the baseband signal is linearly related to n when R_{lt} is constant in time. Since the sequence of sub-pulses can be viewed as frequency samples of the total radar bandwidth in the frequency domain, the 1-D IFFT with respect to can be adopted to achieve the range compression, i.e., the reconstruction of HRRPs. However, due to the translation and the rapidly periodic rotation, R_{lt} is time-varying and the peak position of HRRPs changes with respect to the time series. The phase of the returned signal at sampling time instant $t = mNT_R + nT_R$ is

$$
\begin{aligned}
\phi_l &= \frac{4\pi f_n R_{lt}}{c}\Big|_{t=mNT_R+nT_R} \\
&= \frac{4\pi f_n}{c}[R_{l0} + v(mNT_R + nT_R) \\
&\quad - r_l \cos(\omega(mNT_R + nT_R) + \phi_{l0})] \quad (3)
\end{aligned}
$$

where $m = 0, 1, 2, \ldots, M-1$ denotes the m-th burst and T_R denotes the pulse repetition interval (PRI). The peak positions of HRRPs are determined by

$$
\begin{aligned}
k &= \frac{1}{2\pi}\frac{d\phi_l}{n} \\
&= \frac{2\Delta f R_{l0} + 2f_0 v T_R \cos\theta + 2mNv\Delta f T_R \cos\theta}{c} \\
&\quad + \frac{4nv\Delta f T_R \cos\theta}{c} \\
&\quad - \frac{2\Delta f r_l}{c}\cos(\omega(mNT_R + nT_R) + \phi_{l0}) \\
&\quad + \frac{2f_0 r_l \omega T_R}{c}\sin(\omega(mNT_R + nT_R) + \phi_{l0}) \\
&\quad + \frac{2n r_l \Delta f \omega T_R}{c}\sin(\omega(mNT_R + nT_R) + \phi_{l0}) \quad (4)
\end{aligned}
$$

In the case of rapidly periodic rotating targets illuminated by a conventional FSS radar, $\omega n T_R$ is usually very small and $\cos(\omega n T_R) \approx 1$ and $\sin(\omega n T_R) \approx 0$. Ignoring the last coupling term which is usually negligibly small in (4), the peak positions of HRRPs can be approximately rewritten as

$$
\begin{aligned}
k(m) &= \frac{2(\Delta f R_{l0} + f_0 v T_R \cos\theta)}{c} + \frac{2mNv\Delta f T_R \cos\theta}{c} \\
&\quad + \frac{2\Delta f r_l}{c}\sqrt{1 + \frac{f_0^2\omega^2 T_R^2}{\Delta f^2}}\sin(\omega mNT_R + \phi_{l0} - \varepsilon)
\end{aligned}
$$

$$
\begin{aligned}
&= k_0 + k_1 + r_1 \sin(\omega mNT_R + \phi_{l\varepsilon0}) \\
&= k_0 + k_1 + k_2 \quad (5)
\end{aligned}
$$

Where

$$
\begin{aligned}
k_0 &= \frac{2(\Delta f R_{l0} + f_0 v T_R \cos\theta)}{c} \\
k_1 &= \frac{2mNv\Delta f T_R \cos\theta}{c} \\
r_1 &= \frac{2\Delta f r_l}{c}\sqrt{1 + \frac{f_0^2\omega^2 T_R^2}{\Delta f^2}} \\
k_2 &= r_1 \sin(\omega mNT_R + \phi_{l\varepsilon0}) \\
\phi_{l\varepsilon0} &= \phi_{l0} - \varepsilon, \text{ and} \\
\varepsilon &= \arcsin\left(1/\sqrt{1 + \frac{f_0^2\omega^2 T_R^2}{\Delta f^2}}\right) \quad (6)
\end{aligned}
$$

The first term k_0 in (2) is a constant, the second term k_1 is the first order term with respect to m which imposes a linear modulation on the peak positions of HRRPs in the slow-time-range plane and the last term k_2 is the sinusoidal term which further imposes a sinusoidal modulation on the peak positions of HRRPs. The signal model in (5) can be simplified down to that in [5] when $v = 0$. When $v \neq 0$, the feature extraction method proposed in [5] based on three-point model will be invalid since the curves of HRRPs are not sinusoids anymore. Thus, new feature extraction methods via HRRPs are extremely needed in this new situation.

As demonstrated in the Appendix-A, $k(m + M_T)$ (where M_T is the period of time series) is actually a circular shift form of $k(m)$ and HRRPs perform a circular periodicity with a period of T_d, the same with the m-D modulation period.

III. FEATURE EXTRACTION

Ignoring the induced phase terms, the peak positions of HRRPs of the scattering center l have a simplified and generalized form as

$$|H_l(k, m)| \approx \rho_l \delta(k - (k_0 + k_1 + k_2)) \quad (7)$$

where ρ_l is a constant. Letting $m = m + M_T$, we have

$$
\begin{aligned}
|H_l(k, m + M_T)| &= \rho_l \delta(k - k_0 - k_1 \\
&\quad - r_1 \sin(2\pi + \omega mNT_R + \phi_{l\varepsilon0}) \\
&\quad - 2NM_T v\Delta f T_R \cos\theta/c) \\
&= \rho_l \delta(k - k_0 - k_1 \\
&\quad - r_1 \sin(\omega mNT_R + \phi_{l\varepsilon0}) \\
&\quad - 2NM_T v\Delta f T_R \cos\theta/c) \quad (8)
\end{aligned}
$$

A. CC AND CAMD COEFFICIENTS [10], [31]

As shown in the Appendix-B, the CC coefficients matrix $\mathbf{M}_C$ preserves the periodicity in row and column dimensions. Then the lag in the same diagonal of the CC coefficients matrix $\mathbf{M}_C$ is a constant and elements in the same diagonal are supposed to be almost equivalent. Define the average CC coefficients as the average of p-th diagonal of the matrix

$$C(p) = \text{mean}(\text{diag}(\mathbf{M}_C, p)) \quad (9)$$

where

$$\text{diag}\left(\mathbf{M}_C, p\right) = \{\mathbf{M}_C\left(m_1, m_2\right), m_2 = m_1 + p,$$
$$1 \le m_1 \le M, 1 \le m_2 \le M\} \quad (10)$$

Apparently, $C\left(p\right)$ has the same periodicity and shows peaks at time instant iM_T, $i = 0, \pm 1, \pm 2, \cdots$.

Similarly, as shown in the Appendix-C, the CAMD coefficients matrix $\mathbf{M}_D$ also preserves the periodicity in row and column dimensions. Then the lag in the same diagonal of the CAMD coefficients matrix $\mathbf{M}_D$ is also a constant and elements in the same diagonal are supposed to be almost equivalent. Like the definition of the average CC coefficients, the average CAMD coefficients can be defined as

$$D\left(p\right) = \text{mean}\left(\text{diag}\left(\mathbf{M}_D, p\right)\right) \quad (11)$$

where

$$\text{diag}\left(\mathbf{M}_D, p\right) = \{\mathbf{M}_D\left(m_1, m_2\right), m_2 = m_1 + p,$$
$$1 \le m_1 \le M, 1 \le m_2 \le M\} \quad (12)$$

Similarly, $D\left(p\right)$ has the same periodicity and shows valleys at position iM_T, $i = 0, \pm 1, \pm 2, \cdots$.

Thus, to estimate the rotating m-D frequency is equivalent to extract the intervals of the peaks of $C\left(p\right)$ or the intervals of the valleys of $D\left(p\right)$.

B. EXTRACTION STEPS AND COMPUTATIONAL COMPLEXITY

The rotating frequency can be estimated from the intervals of peaks of the CC coefficients or the intervals of the valleys of the CAMD coefficients. The concrete steps of the rotating frequency estimation method are enumerated in the following list.

Step 1) Reconstruct HRRPs of rotating targets in FSS via FFT, i.e., $H_l\left(k, m\right)$.

Step 2) Calculate the CC coefficients matrix $\mathbf{M}_C$ of $|H_l\left(k, m\right)|$ via (25) in the Appendix-B or calculate the CAMD coefficients matrix $\mathbf{M}_D$ via (33) in the Appendix-C.

Step 3) Calculate the average CC coefficients $C\left(p\right)$ via (6) or calculate the average CAMD coefficients $D\left(p\right)$ via (15).

Step 4) Estimate the intervals of peaks of the average CC coefficients or the intervals of valleys of the average CAMD coefficients.

Step 5) Yield an estimate of rotating period $\hat{T}_d$ by averaging the estimations of intervals and $\hat{f}_d = 1/\hat{T}_d$.

The computational complexity of estimated $\hat{T}_d$ primarily relies on the calculation of $\mathbf{M}_C$ or $\mathbf{M}_D$. There are times multiplication to calculate each $C\left(m_1, m_2\right)$ and $M \times M \times N$ times multiplication to calculate $\mathbf{M}_C$. There are times subtraction to calculate each $D\left(m_1, m_2\right)$ and $M \times M \times N$ times subtraction to calculate $\mathbf{M}_D$. The computational complexity of rotating frequency estimation via the CC coefficients and the CAMD coefficients will be compared with each other later in the simulated trials.

IV. SIMULATIONS

From Section IV-A to IV-D, the characteristics of reconstructed HRRPs of rapidly periodic rotating targets with translation motion in FSS are revealed. Then in Section IV-E, the estimation of rotating rotor blades of helicopters without translation motion is also presented.

TABLE 1. The simulation parameters.

f_d	5 Hz and 7Hz	θ	0 degree
r_l	[0.1, 0.4, 0.9, 1.0, 2.3] m	f_0	30 GHz
σ_l	[0.7, 1.0, 0.9, 0.7,0.8] m^2	Δf	2 MHz
ϕ_{l0}	[0,15, 115, 207, 287] degree	T_R	25×10^{-6} s
v	80 m/s	M	128
R_0	150 m	N	256

In Section IV-A~IV-D, two sets of f_d (5Hz and 7Hz) are chosen in the following simulations and the translation velocity is set to be nonzero for a more general case. According to the electromagnetic (EM) scattering model in high frequency, for a real complex target, the radar echo signal can be decomposed into multiple point scattering centers neglecting the interaction effect of EM scattering. Suppose that there are five strong scattering centers on the moving targets with different rotating radii and scattering coefficients. The main simulation parameters are listed in Table 1.
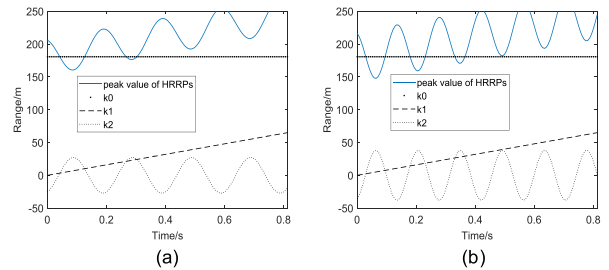

FIGURE 2. Peak values of HRRPs, k_0, k_1 and k_2, (a) f_d=5 Hz. (b) f_d=7 Hz.

Choose the fifth scattering center (r_l = 2.3 m, σ_l = 0.8 m^2, and ϕ_{l0} = 287 degree) for the purpose of illumination, the ideal peak positions of HRRPs when f_d = 5 Hz and f_d = 7 Hz are shown in Figure 2(a) and Figure 2(b), respectively. As depicted in the two figures, each curve of the peak values can be decomposed into k_0, k_1 and k_2, where k_0 is a straight line with zero slope represented by a dotted line, k_1 is a slash represented by a long dash line and k_2 is a sinusoid represented by a short dash line. The simulation results are in accordance with the theoretical analysis in equation (6). And it can also be seen that the sinusoidal periodicity of HRRPs is disturbed by the first order term k_1 induced by the translation motion in both two figures. The whole observation time is about $M \times N \times T_R \approx 0.874$ s which implies that there are four peaks in the CC coefficients or four valleys in

the CAMD coefficients when $f_d = 5$ Hz and five peaks in the CC coefficients or five valleys in the CAMD coefficients when $f_d = 7$ Hz.
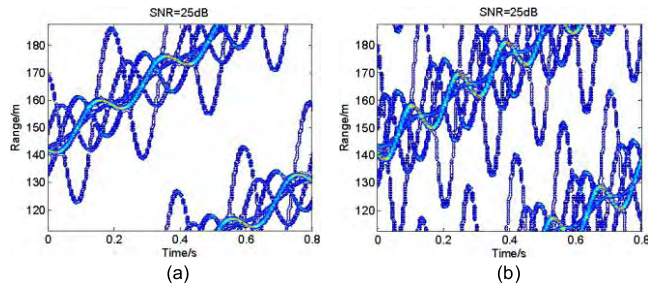

FIGURE 3. HRRPs of the rapid rotating targets with different m-D frequencies with translation motion. (a) f_d=5 Hz. (b) f_d=7 Hz.

The HRRPs of the rapid rotating targets with $f_d = 5$ Hz and 7 Hz but moving at a constant speed $v = 80$ m/s under SNR=25 dB in FSS radar are shown in Figure 3(a) and Figure 3(b), respectively. Just as depicted in the figures, the HRRPs are wrapped in the time-range plane since the rotating frequency is extraordinarily high [5]. It can also be seen that HRRPs of the scattering centers are not normal sinusoidal curves due to the translation motion but with circular periodicity yet; because of this, the conventional feature extraction methods such as three-point model, Hough Transform (HT) or Extended Hough Transform (EHT) may be ineffective or with a huge computational burden.

To demonstrate the extraction of the rotating frequency from the HRRPs, the estimations via the CC coefficients and the CAMD coefficients are presented in following simulations. The precision of the estimations of the two extraction methods are compared with that of EHT and the robustness is also validated from the following simulations with various SNRs. The computational complexity is revealed by the time consumed for rotating frequency estimation.
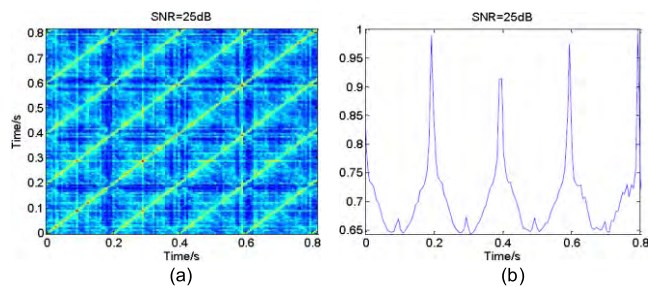

FIGURE 4. Estimated results via CC (f_d=5 Hz and SNR=25 dB). (a) CC coefficients matrix. (b) average CC coefficients.

A. ESTIMATED RESULTS BASED ON THE CC COEFFICIENTS

The CC matrix of the HRRPs in Figure 3(a) when $f_d = 5$Hz is shown in Figure 4(a) and the average CC coefficients are shown in Figure 4(b) which reach four peaks at 0.192 s, 0.3968 s, 0.5952 s and 0.7936 s. The intervals of the peaks
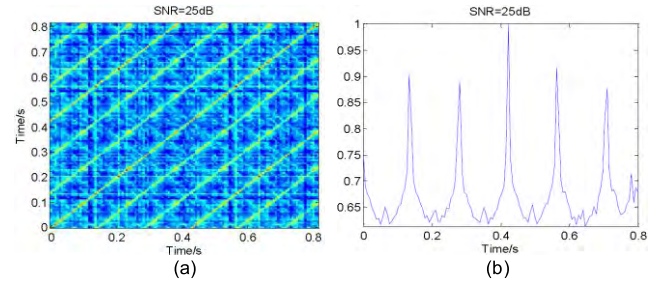

FIGURE 5. Estimated results via CC (f_d=7 Hz and SNR=25 dB). (a) CC coefficients matrix. (b) average CC coefficients.

yield an estimate $\hat{T}_d = 0.1968$ s and $\hat{f}_d = 5.0813$ Hz with a relative error of 1.63%.

The CC matrix of the HRRPs in Figure 3(b) when $f_d = 7$Hz is shown in Figure 5(a) and the average CC coefficients are shown in Figure 5(b) which reach five peaks at 0.1344 s, 0.2816 s, 0.4224 s, 0.5632 s and 0.7104 s. The intervals of the peaks yield an estimate $\hat{T}_d = 0.1398$s and $\hat{f}_d = 7.1543$Hz with a relative error of 2.2%.

From the estimated results of simulated data with high SNR, it can be concluded that the CC matrix presents periodicity in row and column dimensions and the rotating frequency can be estimated accurately via the CC coefficients of HRRPs.
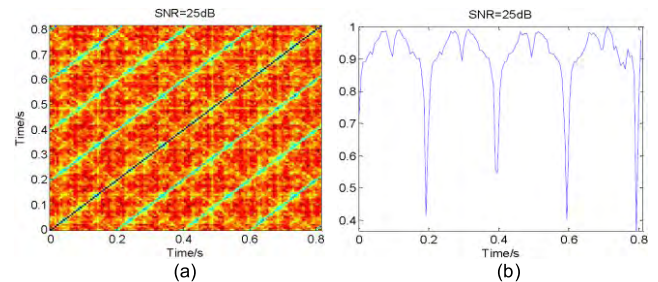

FIGURE 6. Estimated results via CAMD (f_d=5 Hz and SNR=25 dB). (a) CAMD coefficients matrix. (b) average CAMD coefficients.

B. ESTIMATED RESULTS BASED ON THE CAMD COEFFICIENTS

The CAMD matrix of the HRRPs in Figure 3(a) when $f_d = 5$Hz is shown in Figure 6(a) and the average CAMD coefficients are shown in Figure 6(b) which reach four valleys at 0.192 s, 0.3968 s, 0.5952 s and 0.7936 s. The intervals of the valleys yield an estimate $\hat{T}_d = 0.1968$ s and $\hat{f}_d = 5.0813$ Hz with a relative error of 1.63% which are the same as the estimation from CC coefficients.

The CAMD matrix of the HRRPs in Figure 3(b) when $f_d = 7$Hz is shown in Figure 7(a) and the average CC coefficients are shown in Figure 7(b) which reach five valleys at 0.1344 s, 0.2816 s, 0.4224 s, 0.5632 s and 0.7104 s. The intervals of the valleys yield an estimate $\hat{T}_d = 0.1398$s and $\hat{f}_d = 7.1543$Hz with a relative error of 2.2% which are also the same as the estimation from CC coefficients.

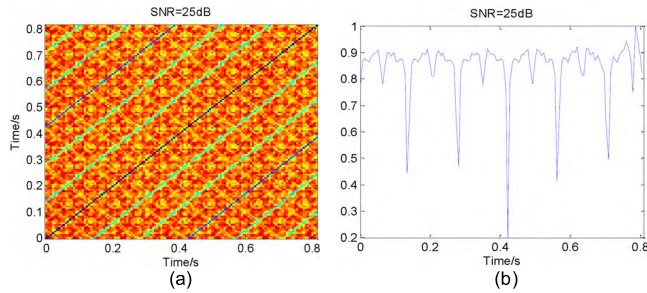Although the rotating frequencies extracted from HRRPs based on the two extraction methods are with the same

FIGURE 7. Estimated results via CAMD (f_d=7 Hz and SNR=25 dB). (a) CAMD coefficients matrix. (b) average CAMD coefficients.
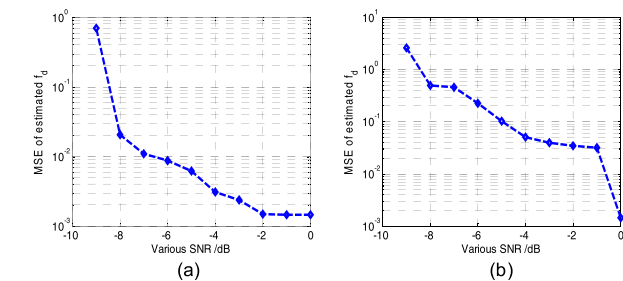

FIGURE 8. MSE of $\hat{f}_d$ in various SNR. (a) via CC coefficients. (b) via CAMD coefficients.

precision under SNR=25 dB, it should be noticed that a high SNR is presented in the above simulations which may be not accord with the real scenarios. To reveal the robustness of the two methods, simulations with different SNRs are presented in the following.

C. ESTIMATED RESULTS IN VARIOUS SNRS

To prove the robustness of the two extraction methods in a more realistic scenario, simulations with Gaussian distributed complex noise in different SNRs (0 dB, −5 dB, −8 dB and −9 dB) when $f_d = 5$ Hz are presented here. The additive Gaussian noise with given SNR is added into the simulated radar echo of each burst, i.e. m, as follows,

Step 1) Let $m = 0$ and simulate the radar echo with $s(n, m)$ the signal amplitude assumed to be 1 Voltage. The power of the simulated radar echo of the m-th burst (without noise) can be calculated as

$$P_m = \sum_{n=0}^{N-1} s^2(n, m) \tag{13}$$

Step 2) For a given SNR (units in dB), the variance of noise can be calculated as

$$Var = \frac{P_m}{10^{\frac{SNR}{10}}} \tag{14}$$

Step 3) The complex noise can be simulated as

$$\text{Noise}(n, m) = \text{hilbert}\left(\sqrt{Var} \times \text{randn}(n, m)\right) \tag{15}$$

where $\text{hilbert}(\cdot)$ computes the so-called analytic signal and $\text{randn}(\cdot)$ returns a matrix containing pseudorandom values
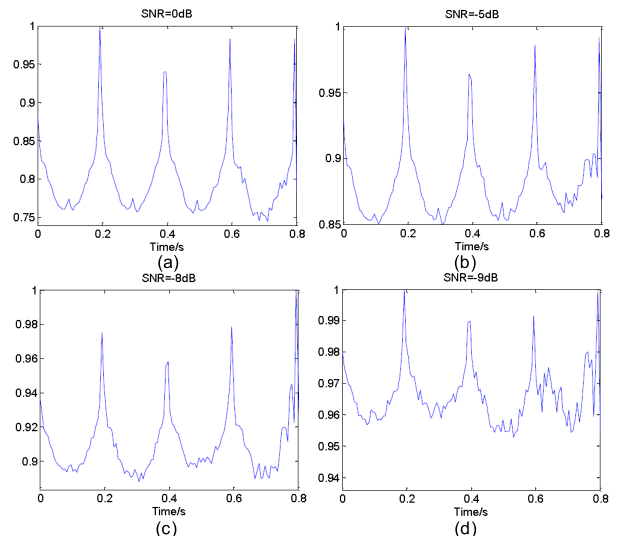

FIGURE 9. Estimated results with various SNR based on CC coefficients. (a) 0 dB. (b) −5 dB. (c) −8 dB. (d) −9 dB.
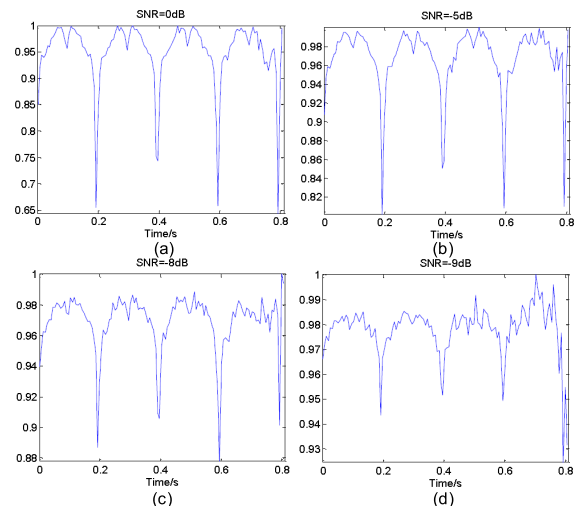

FIGURE 10. Estimated results with various SNR based on CAMD coefficients. (a) 0 dB. (b) −5 dB. (c) −8 dB. (d) −9 dB.

drawn from the standard normal distribution. Then the finally simulated radar echo is

$$s'(n, m) = s(n, m) + \text{Noise}(n, m) \tag{16}$$

Step 4) Repeat Step 1) to Step 3) with the increase of until $m = M - 1$.

The corresponding CC coefficients and the CAMD coefficients are shown in Figure 9 and Figure 10, respectively. The estimated $\hat{f}_d$s and the relative errors are given in Table 2.

The results are mean values calculated for a few independent measurements using Monte Carlo simulation (100 times). The mean squared errors (MSE) of $\hat{f}_d$ via CC and CAMD coefficients in various SNR are plotted in Figure 8(a) and Figure 8(b), respectively.

From the estimated MSE shown in Figure 8(a) and the CC coefficients shown in Figure 9(a)~(d), the peaks of CC

TABLE 2. Estimated results.

	CC		CAMD	
	$\hat{f}_d$ (Hz)	relative error (%)	$\hat{f}_d$ (Hz)	relative error (%)
0dB	4.9115	1.77	4.9115	1.77
-5dB	4.9111	1.78	4.9111	1.78
-8dB	4.8675	2.65	4.8005	4.8005
-9dB	4.7215	5.57	4.6835	6.33

coefficients are not obvious when the SNR decreases seriously. As depicted in Table 2, when SNR=−8 dB the rotating frequency estimation is 4.8675 Hz with a relative error of 2.65% and the MSE of $\hat{f}_d$ is about $10^{-1.69}$ which is almost acceptable. When SNR=−9 dB, the peaks are contaminated by the additive Gaussian distributed noise and the rotating frequency estimation sunk to 4.7215 Hz with a relative error of 5.57% and the MSE of $\hat{f}_d$ is about $10^{-1.25}$ which is already relatively poor.

From the estimated MSE shown in Figure 8(b) and the CAMD coefficients shown in Figure 10(a)∼(d), the valleys of CAMD coefficients are also not obvious when the SNR decreases seriously. The rotating frequency estimation is 4.8005 Hz with a relative error of 3.99% and the MSE of $\hat{f}_d$ is about $10^{-1.4}$ when SNR=−8 dB. When SNR=−9 dB, the peaks are already contaminated by the noise and not easy to identify and the number of valleys increases to five and the last one is a fake. The rotating frequency estimation sunk to 4.6835 Hz with a relative error of 6.33% and the MSE of $\hat{f}_d$ also degraded to $10^{-1.19}$.

Compared the estimated results with each other, we can see that the estimated $\hat{f}_d$ via the CC and CAMD coefficients is good enough when SNR is no less than −8 dB. But from the MSE of estimated rotating frequency in Figure 8, it can be concluded that the rotating frequency extraction via the CC coefficients is more robust than that via the CAMD coefficients in low SNRs. Besides these characteristics, the time consumed for rotating frequency estimation via the CC coefficients is also less than that via the CAMD coefficients, which will be demonstrated in the following.

D. COMPUTATIONAL COMPLEXITY

To validate the accuracy and efficiency of the two proposed estimation algorithms compared to the conventional works, EHT is utilized to extract the m-D parameters from HRRPs. The location of scattering center in the range domain can be scaled by dividing $k(m)$ by $2\Delta f/c$ in equation (5), i.e.,

$$R_l(m) = R_{l0}\frac{f_0 T_R \cos\theta}{\Delta f} + mNvT_R\cos\theta$$
$$+ r_l\sqrt{1 + \frac{f_0^2\omega^2 T_R^2}{\Delta f^2}}\sin(\omega mNT_R + \phi_{l\varepsilon 0})$$
$$= R_l^* + r^*\sin(\omega mNT_R + \phi_{l\varepsilon 0}) \qquad (17)$$
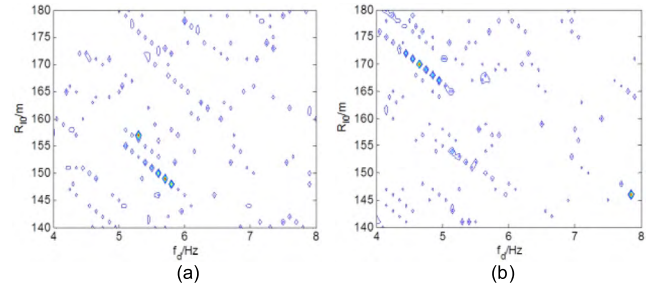

FIGURE 11. Estimated f_d against R_{l0} estimated via six-parameter EHT. (a) f_d=5 Hz. (b) f_d=7 Hz.
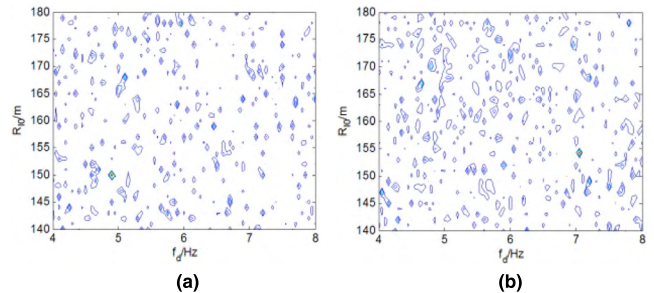

FIGURE 12. Estimated f_d against estimated R_{l0} via four-parameter EHT (SNR=0 dB). (a) f_d=5 Hz. (b) f_d=7 Hz.

where $R_l^* = R_{l0}\frac{f_0 T_R\cos\theta}{\Delta f} + mNvT_R\cos\theta$ and $r^* = r_l\sqrt{1 + \frac{f_0^2\omega^2 T_R^2}{\Delta f^2}}$.

The constructed six-parameter EHT equation to extract the m-D parameters $(R_{l0}; f_d; r^*; \phi_{l\varepsilon 0}; v; \theta)$ is as follows

$$R_{l0} = R_l(m) - r^*\sin(2\pi f_d mNT_R + \phi_{l\varepsilon 0})$$
$$- \frac{f_0 vT_R\cos\theta}{\Delta f} - mNvT_R\cos\theta \qquad (18)$$

The estimated parameters via the six-parameter EHT are partly shown in Figure 11 in which SNR=0 dB. When $f_d = 5$ Hz, the estimated m-D frequency f_d in the parameter domain of the six-parameter EHT is shown in Figure 11(a) in which it is clearly that the estimations run into local optimums at 5.3 Hz, 5.7 Hz and 5.8 Hz. When $f_d = 7$ Hz, the estimations run into local optimums at 4.45 Hz, 4.55 Hz, 4.65 HZ, 4.75 Hz, 4.85 Hz, 4.95 Hz and 7.85 Hz.

To remove the local optimums and the cost burden, the velocity v is assumed to be zero and the parameter dimensions of EHT are reduced to four. Then the four-parameter EHT equation to extract the m-D parameters $((R_{l0}; f_d; r^*; \phi_{l\varepsilon 0}))$ is as follows

$$R_{l0} = R_l(m) - r^*\sin(2\pi f_d mNT_R + \phi_{l\varepsilon 0}) \qquad (19)$$

The estimated parameters via the four-parameter EHT are partly shown in Figure 12 and the peak value yields an

estimation of m-D frequency. When $f_d = 5$ Hz, the estimated m-D frequency f_d in the parameter domain of the four-parameter EHT shown in Figure 12(a) in which it is clearly that the estimation equals 4.9 Hz with a relative error of 2% and when $f_d = 7.1$ Hz, the estimation is 7.1 Hz with a relative error of 1.4% as shown in Figure 12(b). The estimations are accurate by the four-parameter EHT. The results imply that the precision of EHT-based parameter estimation method is limited when the parameter dimension increases.
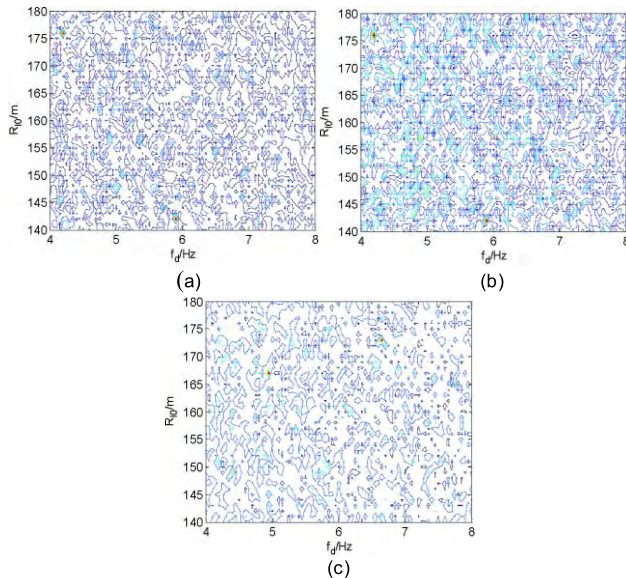

FIGURE 13. Estimated f_d against estimated R_{I0} via four-parameter EHT under various SNRs. (a) SNR=−5 dB. (b) SNR=−8 dB. (c) SNR=−9 dB.

Another three groups of feature extractions via the four-parameter EHT with different SNRs (−5 dB, −8 dB and −9 dB) are conducted to illuminate the effect compared to that via the CC and CAMD coefficients. The estimated m-D frequency f_d via the four-parameter EHT under various SNRs are partly shown in Figure 13. When SNR=-5 dB, $\hat{f}_d = 5.9$ Hz with a relative error of 18% which is not acceptable, as shown in Figure 13(a). When SNR=−8 dB and −9dB, as shown in Figure 13(b) and Figure 13(c), the peaks are contaminated by the noise and the estimations are also out of true.

To demonstrate the computational complexity of the two extraction methods compared with the four-parameter EHT, simulations with $f_d = 5$ Hz with various M(128, 256 and 512) are presented here. In the same system and hardware condition, which includes a 64-bit Windows®7 SP1 OS, an Intel®Core i7-6500U 2.5 GHz CPU, a 1-MB L2 cache, and an 8192-MB memory capacity, the time consumed for rotating frequency estimation via the CC coefficients, the CAMD coefficients and the four-parameter EHT is given in Table 3.

The matrix of HRRPs is a 128×256 matrix when $M = 128$, a 256×256 matrix when $M = 256$, and a 512×256 matrix when $M = 512$. The CAMD coefficients calculation from

TABLE 3. Time consumed for estimation.

M	CC	CAMD	four-parameter EHT
128	0.94 s	79.26 s	22.65 s
256	2.83 s	98.61 s	48.98 s
512	13.58 s	436.33 s	93.89 s

a huge matrix is very expensive in terms of computational time while the CC coefficients can be calculated by the fast algorithm of circular convolution. Thus, the efficiency of rotating frequency estimation via the CC coefficients is usually very high which is proven in Table 3. The computational time of estimations via the four-parameter EHT is more than that of estimations via the CC coefficients and less than that of estimations via the CAMD coefficients. However, the EHT easily runs into local optimums when the parameter dimensions increase which leads to inadequate estimations as shown in Figure 11.

Thus, in general, in the cases of SNR no less than -8 dB, rotating frequency extractions via the CC coefficients and the CAMD coefficients are both acceptable with high accuracy compared with that via the EHT, but estimation method via the CC coefficients is more efficient than that via the EHT and the CAMD coefficients. In low SNR cases, the extraction method via the CC coefficients is not only accurate but also efficient compared to that via the EHT and the CAMD coefficients. Although the extraction efficiency via the CAMD coefficients is much lower than that via the CC coefficients, its accuracy under SNR no less than -8 dB is validated and it is more reliable than high-dimensional EHT which easily runs into local optimums. The rotating frequency estimation via the CAMD coefficients does enrich the methods of m-D feature extraction and the fast algorithm to calculate the CAMD coefficients matrix is a potential direction in further researches.

E. ESTIMATED RESULTS OF ROTATING ROTOR BLADES
For real rotating rotor blades of helicopters, the rotation rate is nearly from one to a few revolutions/second (r/s), typically 1-9 r/s, i.e., $f_d = 1$-9 Hz. For example, the rotating rate of USA Air Force Bell AH-1 helicopter, also known as "Huey Cobra", is 4.9 r/s with $f_d = 4.9$ Hz. For this reason, the simulated data utilized in [27] is chosen here to validate the effect of the proposed rotating frequency estimation algorithms via the CC and the CAMD coefficients in this paper. In the simulations, the radar is supposed to be at C-band with a wavelength of 0.06 m and a bandwidth of 300 MHz. The length of rotor blades is about 6.5 m. The rotation rate $f_d = 4$ Hz, the translation velocity of the helicopter is about 100m/s and the range from the radar to the center of the rotor is about 750 m [27]. The HRRPs of the two-blade rotating rotor and the three-blade rotating rotor without translation motion are presented in Figure 14(a) and Figure 14(b), respectively [27].
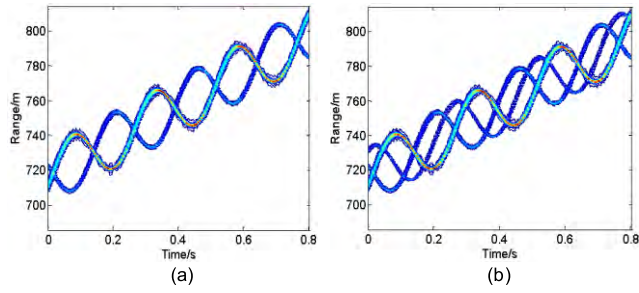
FIGURE 14. HRRPs of the rotating rotor blades with various number of blades. (a) two-blade rotating rotor. (b) three-blade rotating rotor.
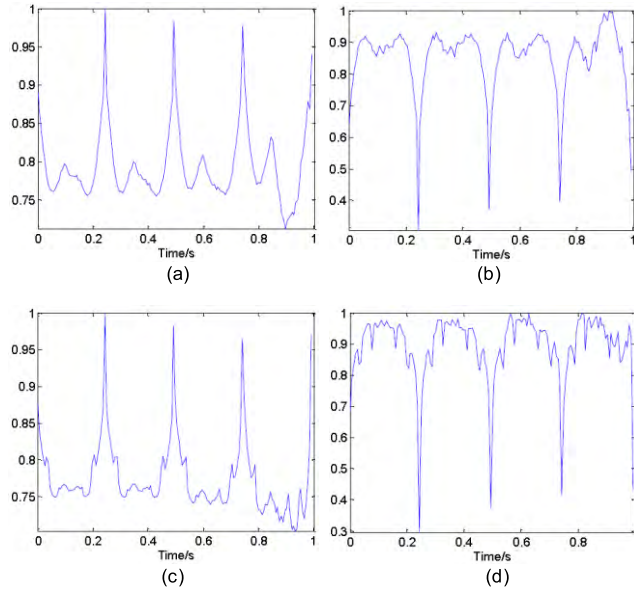

FIGURE 15. Estimated results of rotating rotor blades. (a) CC coefficients of two-blade rotor. (b) CAMD coefficients of two-blade rotor. (c) CC coefficients of three-blade rotor. (d) CAMD coefficients of three-blade rotor.

The average CC coefficients and the average CAMD coefficients of two-blade rotating rotor are shown in Figure 15(a) and Figure 15(b) while that of three-blade rotating rotor are shown in Figure 15(c) and Figure 15(d), respectively.

In Figure 15(a) and Figure 15(c), the average CC coefficients reaches its three peaks at 0.2431 s, 0.4929 s and 0.7425 s and the intervals of the peaks yields an estimate $\hat{T}_d = 0.2457$ s and $\hat{f}_d = 4.0702$ Hz with a relative error of 1.76%. In Figure 15(b) and Figure 15(d), the average CAMD coefficients also reaches its three valleys at 0.2433 s, 0.4929 s and 0.7424 s and the intervals of the peaks yields an estimate $\hat{T}_d = 0.2457$ s and $\hat{f}_d = 4.0702$ Hz with a relative error of 1.76%. The estimations from the HRRPs of the rotating rotor blades of helicopters without translation motion also demonstrate the effectiveness of the proposed algorithms based on the CC and CAMD coefficients under high SNRs.

V. EXPERIMENTAL RESULTS
In this section, experimental trials of rotating targets are conducted to prove the validity of the m-D frequency extraction

FIGURE 16. Outfield experiments of rotating targets. (a) FSS radar and the scenario of the outfield experiments. (b) Rotating targets.
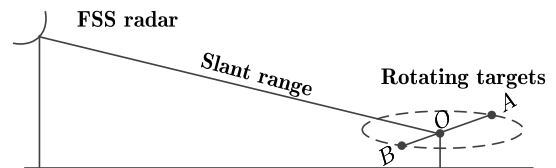

FIGURE 17. Geometry of the outfield experiments.

methods. The FSS radar works in millimeter wave band with a wavelength of 0.8 cm and a peak power no less than 1.5 watt. The conformal antenna is a planar slot array antenna with an aperture of 152 mm. The main parameters of the FSS radar are as follows: $f_c = 37.5$ GHz, $T_R = 20$ μs, $\Delta f = 0.5$ MHz and with a totally bandwidth 512 MHz. Thus, we have that $N = 512/\Delta f = 1024$ and the range resolution is about 0.5 m.

The scenario of the outfield experiments is shown in Figure 16(a). The rotating target consists of two metal trihedral corner reflectors connected by a wooden spiral arm and the center of rotation is in the center of the wooden spiral arm. The rotating target is driven by a rotary motor and has been placed on the ground with a translation velocity $v = 0$ m/s and radius $r_A = r_B = 0.4$ m as shown in Figure 16(b) [5]. The geometry of the outfield experiments is shown in Figure 17. Since the rotating target has been placed on the ground, the FSS radar is set up on a high distance for vision. On the other hand, the slant range between the center of rotation O and the FSS radar is about 160 m to fulfill the far field assumption.

The main interference in the scenario is the inevitable ground clutter when the FSS radar looks down upon the ground which can be cancelled by the method proposed in [23]. The original HRRPs of rotating targets with $f_d = 1.61$ Hz are illustrated in Figure 18(a) which can be seen that HRRPs are contaminated with strong ground clutter and the HRRPs after the first-order ground clutter cancellation are shown in Figure 18 (b) [5].

It is difficult to track moving targets in the scenario mentioned above, so there is no translation motion in the original measured data of the rotating targets. But it is easy to add the phases induced by the translation motion into the measured data. The phases can be extracted from equation (3) in section II which is $\frac{4\pi f_n}{c} v (mNT_R + nT_R) \cos \theta$. The velocity
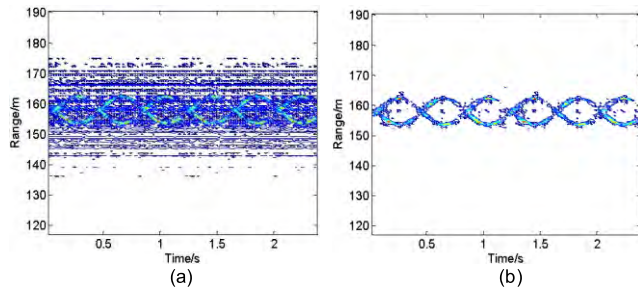
FIGURE 18. HRRPs of rotating targets. (a) Original HRRPs. (b) HRRPs after clutter cancellation.
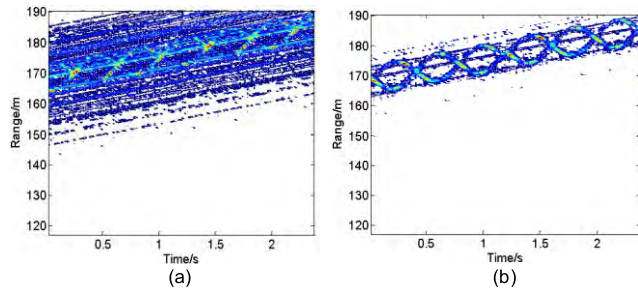

FIGURE 19. HRRPs of rotating targets with translation motion added. (a) Original HRRPs with translation motion added. (b) HRRPs with translation motion added after clutter cancellation.

FIGURE 20. Estimated results of real data (f_d=1.61 Hz). (a) average CC coefficients. (b) average CAMD coefficients. (c) estimations via the four-parameter EHT.

TABLE 4. The true values and estimated results of rotating frequency.

Experiment No.	1	2	3	4
real f_d (Hz)	1.39	1.26	1.32	1.49
$\hat{f}_d$ (Hz) via CC	1.36 (2.16%)	1.25 (0.79%)	1.30 (1.52%)	1.46 (2.01%)
$\hat{f}_d$ (Hz) via CAMD	1.36 (2.16%)	1.27 (0.79%)	1.29 (2.27%)	1.49 (0.67%)
$\hat{f}_d$ (Hz) via EHT	1.34 (3.60%)	1.23 (2.38%)	1.35 (2.27%)	1.51 (1.34%)

of translation motion is set to be 14 m/s and $\theta = 60$ degree without loss of generality.

The HRRPs of rotating targets with translation motion are shown in Figure 19(a). The HRRPs are slanted compared with the original HRRPs shown in Figure 18(a) after the phases induced by the translation motion are added into the real data. The HRRPs of rotating targets with translation motion added after the first-order ground clutter cancellation are shown in Figure 19 (b). From Figure 19(b) it can also be seen that although the scattering strength of each scattering center changes with time and the scattering blinking when the target is rotating, the circular periodicity of HRRPs is still preserved.

The average CC coefficients of the HRRPs with translation motion are shown in Figure 20(a) which reaches its three peaks at 0.5939 s, 1.229 s and 1.864 s. The intervals of the peaks yield an estimate $\hat{T}_d = 0.6099$ s and $\hat{f}_d = 1.64$ Hz with a relative error of 1.9%. The average CAMD coefficients is shown in Figure 20(b) which reaches its three valleys at 0.6144 s, 1.229 s and 1.864 s. The intervals of the valleys yield an estimate $\hat{T}_d = 0.6167$ s and $\hat{f}_d = 1.62$ Hz with a relative error of 0.62%. The estimated parameters via the four-parameter EHT are partly shown in Figure 20(c) in which it is clearly that the estimation equals 1.54 Hz with a relative error of 4.35%.

Another four groups of experiments with different values of rotating frequencies are also performed. The true values of f_d in each experiment and the estimated results $\hat{f}_d$ via the CC coefficients, the CAMD coefficients and the four-parameter EHT can be found in Table 4. The relative errors are also
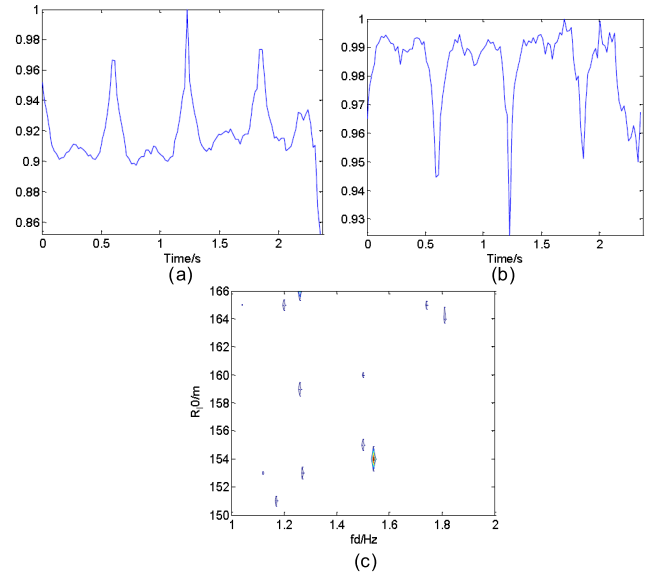
presented in Table 4 in the corresponding bracket of each estimation. From these five groups of outfield experiments of rotating targets, the frequency estimation algorithms based on the CC coefficients and the CAMD coefficients of HRRPs are demonstrated.

VI. CONCLUSION

In this paper, the HRRPs of rotating targets with translation motion in FSS are presented and the rotating frequency is estimated accurately based on the circular periodicity of HRRPs. The novelty of this paper is that it demonstrates the usefulness of the parameter estimation algorithms based on the CC coefficients and the CAMD coefficients of HRRPs with translation motion. From the analytical results, it is shown that the curves of HRRPs cannot be represented as norm sinusoidal modulation due to the translation motion. Based on the analyses, rotating frequency estimation algorithms based on the CC coefficients and the CAMD coefficients of HRRPs, are proposed and compared with each other under simulation trials with different SNRs. The proposed two methods both perform accurately under high SNR conditions while the feature extraction method via the CC coefficients is more efficient. Under low SNR conditions (less than -8 dB), only

the estimation via the CC coefficients have high precision. However, the estimations via the CAMD coefficients performance better than the estimations via the EHT algorithms with high parameter dimensions and the improvement of calculation cost of the CAMD matrix is a potential research field yet.

APPENDIX
A. CIRCULAR PERIODICITY OF HRRPs
To demonstrate the circular periodicity of HRRPs of rotating targets with translation motion, let $m = m + M_T$, giving the following

$$
\begin{aligned}
k(m + M_T) &= k_0 + k_1 + \frac{2NM_T v \Delta f T_R \cos \theta}{c} \\
&\quad + r_1 \sin(\omega(m + M_T)NT_R + \phi_{l\varepsilon0}) \\
&= k_0 + k_1 + r_1 \sin(2\pi + \omega m NT_R + \phi_{l\varepsilon0}) \\
&\quad + \frac{2NM_T v \Delta f T_R \cos \theta}{c} \\
&= k(m) + \frac{2NM_T v \Delta f T_R \cos \theta}{c}
\end{aligned} \tag{20}
$$

where M_T is the period of time series.

Due to the translation motion, i.e., $v \neq 0$, the sinusoidal periodicity of HRRPs is disturbed just as depicted in (20). However, the last term in (20) is constant in each m-D modulation period and $k(m + M_T)$ is a circular shift form of $k(m)$ which means that HRRPs perform a circular periodicity with a period of T_d.

B. CC COEFFICIENTS
The circular cross-correlation of two slices of $H_l(k, m)$ at instant m_1, m_2 is defined as [10]

$$
\begin{aligned}
C_l(q; m_1, m_2) &= \sum_{k=0}^{N-1} |H_l(k, m_1)| \\
&\quad \times |H_l(\mathrm{mod}(k + q), m_2)| \\
&= \sum_{k=0}^{N-1} \rho_l \delta(k - k_0 - k_1 \\
&\quad - r_1 \sin(\omega m_1 NT_R + \phi_{l\varepsilon0})) \\
&\quad \times \rho_l \delta(\mathrm{mod}(k + q) - k_0 - k_1 \\
&\quad - r_1 \sin(\omega m_2 NT_R + \phi_{l\varepsilon0}))
\end{aligned} \tag{21}
$$

Letting $m_2 = m_2 + M_T$

$$
\begin{aligned}
C_l(q; m_1, m_2 + M_T) &= \sum_{k=0}^{N-1} |H_l(k, m_1)| \\
&\quad \times |H_l(\mathrm{mod}(k + q), m_2 + M_T)| \\
&= \sum_{k=0}^{N-1} \rho_l \delta(k - k_0 - k_1 \\
&\quad - r_1 \sin(\omega m_1 NT_R + \phi_{l\varepsilon0})) \\
&\quad \times \rho_l \delta(\mathrm{mod}(k + q) - k_0 - k_1 \\
&\quad - r_1 \sin(\omega m_2 NT_R + \phi_{l\varepsilon0}) \\
&\quad - 2NM_T v \Delta f T_R \cos \theta/c)
\end{aligned} \tag{22}
$$

Letting $\mathrm{mod}(k + \eta) = \mathrm{mod}(k + q) - 2NM_T v \Delta f T_R \cos \theta/c$, then (22) becomes

$$
\begin{aligned}
C_l(\mathrm{mod}(\eta &+ 2NM_T v \Delta f T_R \cos \theta/c); m_1, m_2 + M_T) \\
&= \sum_{k=0}^{N-1} \rho_l \delta(k - k_0 - k_1 \\
&\quad - r_1 \sin(\omega m_1 NT_R + \phi_{l\varepsilon0})) \\
&\quad \times \rho_l \delta(\mathrm{mod}(k + \eta) - k_0 - k_1 \\
&\quad - r_1 \sin(\omega m_2 NT_R + \phi_{l\varepsilon0})) \\
&= C_l(\eta; m_1, m_2 + M_T)
\end{aligned} \tag{23}
$$

According to (22) and (23), it has

$$
\begin{aligned}
C_l(q; m_1, m_2) &= C_l(\mathrm{mod}(\eta + 2NM_T v \Delta f T_R \cos \theta/c); \\
&\quad m_1, m_2 + M_T)
\end{aligned} \tag{24}
$$

It can be seen from (24) that $C_l(q; m_1, m_2 + M_T)$ is the circular shift of $C_l(q; m_1, m_2)$ and the circular cross-correlation of $H_l(k, m)$ preserves the periodicity of $H_l(k, m)$. Then the CC coefficients matrix of $H_l(k, m)$ can be defined as

$$
\mathbf{M}_C = \begin{pmatrix} C(0, 0) & \cdots & C(0, M-1) \\ \vdots & \ddots & \vdots \\ C(M-1, 0) & \cdots & C(M-1, M-1) \end{pmatrix} \tag{25}
$$

where the CC coefficient, $C(m_1, m_2)$, is the normalized maximal value of $C_l(q; m_1, m_2)$, i.e.,

$$
C(m_1, m_2) = \frac{\max_q(C_l(q; m_1, m_2))}{\sqrt{\sum_{k=0}^{N-1} |H_l(k, m_1)|^2} \sqrt{\sum_{k=0}^{N-1} |H_l(k, m_2)|^2}} \tag{26}
$$

According to the definition of $C(m_1, m_2)$, it is easy to prove that

$$
C(m_1, m_2) = C(m_2, m_1), \quad 0 \leq C(m_1, m_2) \leq 1 \tag{27}
$$

Usually, $C(m_1, m_2) = 1$ when $m_2 = m_1 + iM_T$ ($i \in M$), which means that $C(m_1, m_2)$ has the same periodicity with $C_l(q; m_1, m_2)$, i.e.,

$$
C(m_1, m_2) = C(m_1, m_2 + M_T) \tag{28}
$$

Therefore, the CC coefficients matrix preserves the periodicity in row and column dimensions.

C. CAMD COEFFICIENTS
In this segment, we reveal the circular periodicity of the CAMD coefficients. Consider two slices of $H_l(k, m)$ at instant m_1, m_2, the CAMD is defined as [30]

$$
\begin{aligned}
D_l(q; m_1, &m_2 + M_T) \\
&= \sum_{k=0}^{N-1} ||H_l(k, m_1)| - |H_l(\mathrm{mod}(k + q), m_2 + M_T)|| \\
&= \sum_{k=0}^{N-1} |\rho_l \delta(k - k_0 - k_1 \\
&\quad - r_1 \sin(\omega m_1 NT_R + \phi_{l\varepsilon0}))
\end{aligned}
$$

$$- \rho_l \delta \left(\text{mod} \, (k + q) - k_0 - k_1 \right.$$
$$\left. - r_1 \sin \left(\omega m_2 N T_R + \phi_{l\varepsilon 0} \right) \right) | \qquad (29)$$

Letting $m_2 = m_2 + M_T$ yields

$$D_l \left(q; m_1, m_2 + M_T \right) = \sum_{k=0}^{N-1} |\rho_l \delta \left(k - k_0 - k_1 \right.$$
$$- r_1 \sin \left(\omega m_1 N T_R + \phi_{l\varepsilon 0} \right))$$
$$\times \rho_l \delta \left(\text{mod} \, (k + q) - k_0 - k_1 \right.$$
$$- r_1 \sin \left(\omega m_2 N T_R + \phi_{l\varepsilon 0} \right)$$
$$- 2 N M_T v \Delta f T_R \cos \theta / c) | \qquad (30)$$

Letting $\text{mod}(k + \eta) = \text{mod}(k + q) - 2 N M_T v \Delta f T_R \cos \theta / c$, (30) becomes

$$D_l \left(\text{mod} \, (\eta + 2 N M_T v \Delta f T_R \cos \theta / c) ; m_1, m_2 + M_T \right)$$
$$= \sum_{k=0}^{N-1} |\rho_l \delta \left(k - k_0 - k_1 \right.$$
$$- r_1 \sin \left(\omega m_1 N T_R + \phi_{l\varepsilon 0} \right))$$
$$- \rho_l \delta \left(\text{mod} \, (k + \eta) - k_0 - k_1 \right.$$
$$- r_1 \sin \left(\omega m_2 N T_R + \phi_{l\varepsilon 0} \right)) |$$
$$= D_l \left(\eta; m_1, m_2 + M_T \right) \qquad (31)$$

According to (30) and (31), we can get

$$D_l \left(q; m_1, m_2 \right) = D_l \left(\text{mod} \, (\eta + 2 N M_T v \Delta f T_R \cos \theta / c) ; \right.$$
$$\left. m_1, m_2 + M_T \right) \quad (32)$$

From (32)(15), it relates explicitly that that $D_l \left(q; m_1, m_2 + M_T \right)$ is the circular shift of $D_l \left(q; m_1, m_2 \right)$ and CAMD also preserves the periodicity of $H_l \left(k, m \right)$. Then the CAMD coefficients matrix of $H_l \left(k, m \right)$ is denoted by

$$\mathbf{M}_D = \begin{pmatrix} D \left(0, 0 \right) & \cdots & D \left(0, M-1 \right) \\ \vdots & \ddots & \vdots \\ D \left(M-1, 0 \right) & \cdots & D \left(M-1, M-1 \right) \end{pmatrix} \quad (33)$$

where the CAMD coefficients, $D \left(m_1, m_2 \right)$ is the normalized minimal value of $D_l \left(q; m_1, m_2 \right)$, i.e.,

$$D \left(m_1, m_2 \right) = \frac{\min_q \left(D_l \left(q; m_1, m_2 \right) \right)}{\sum_{k=0}^{N-1} \left(|H_l \left(k, m_1 \right)| + |H_l \left(k, m_2 \right)| \right)} \quad (34)$$

It is also easy to prove that

$$D \left(m_1, m_2 \right) = D \left(m_2, m_1 \right), 0 \leq D \left(m_1, m_2 \right) \leq 1 \quad (35)$$

and $C \left(m_1, m_2 \right) = 0$ when $m_2 = m_1 + i M_T$ $(i \in M)$, i.e.,

$$D \left(m_1, m_2 \right) = D \left(m_1, m_2 + M_T \right) \quad (36)$$

$D \left(m_1, m_2 \right)$ has the same periodicity with $D_l \left(q; m_1, m_2 \right)$ and the CAMD coefficients matrix also preserves the periodicity in row and column dimensions.

ACKNOWLEDGMENT

REFERENCES

[1] T. Thayaparan, S. Abrol, E. Riseborough, L. Stankovic, D. Lamothe, and G. Duff, "Analysis of radar micro-Doppler signatures from experimental helicopter and human data," *IET Radar, Sonar Navigat.*, vol. 1, no. 4, pp. 289–299, Aug. 2007.

[2] Y. Kim and H. Ling, "Human activity classification based on micro-Doppler signatures using a support vector machine," *IEEE Trans. Geosci. Remote Sens.*, vol. 47, no. 5, pp. 1328–1337, May 2009.

[3] H. Gao, L. Xie, S. Wen, and Y. Kuang, "Micro-Doppler signature extraction from ballistic target with micro-motions," *IEEE Trans. Aerosp. Electron. Syst.*, vol. 46, no. 4, pp. 1969–1982, Apr. 2010.

[4] A. Balleri, K. Chetty, and K. Woodbridge, "Classification of personnel targets by acoustic micro-Doppler signatures," *IET Radar, Sonar, Navigat.*, vol. 9, no. 5, pp. 943–951, 2011.

[5] X. Y. Pan, W. Wang, D. J. Feng, Y. C. Liu, and G. Y. Wang, "Signature Extraction From Rotating Targets Based on a Fraction of HRRPs," *IEEE Trans. Antennas Propag.*, vol. 63, no. 2, pp. 585–592, Feb. 2015.

[6] W.-G. Dong and Y.-J. Li, "Radar target recognition based on micro-Doppler effect," *Optoelectron. Lett.*, vol. 4, no. 6, pp. 456–459, 2008.

[7] G. E. Smith, K. Woodbridge, and C. J. Baker, "Radar micro-Doppler signature classification using dynamic time warping," *IEEE Trans. Aerosp. Electron. Syst.*, vol. 3, no. 46, pp. 1078–1096, Mar. 2010.

[8] S. Huixia and L. Zheng, "Nutation feature extraction of ballistic missile warhead," *Electron. Lett.*, vol. 47, no. 13, pp. 770–772, 2011.

[9] L. Liu, D. McLernon, M. Ghogho, W. Hu, and J. Huang, "Ballistic missile detection via micro-Doppler frequency estimation from radar return," *Digit. Signal Process.*, vol. 22, pp. 87–95, Jan. 2012.

[10] W. Zhang, K. Li, and W. Jiang, "Parameter estimation of radar targets with macro-motion and micro-motion based on circular correlation coefficients," *IEEE Signal Process. Lett.*, vol. 22, no. 5, pp. 633–637, May 2015.

[11] L. Stankovic, I. Djurovic, and T. Thayaparan, "Separation of target rigid body and micro-doppler effects in ISAR imaging," *IEEE Trans. Aerosp. Electron. Syst.*, vol. 42, no. 4, pp. 1496–1506, Oct. 2006.

[12] F. Zhu, X.-D. Zhang, Y.-F. Hu, and D. Xie, "Nonstationary hidden Markov models for multiaspect discriminative feature extraction from radar targets," *IEEE Trans. Signal Process.*, vol. 55, no. 5, pp. 2203–2214, May 2007.

[13] G. Li and P. K. Varshney, "Micro-Doppler parameter estimation via parametric sparse representation and pruned orthogonal matching pursuit," *IEEE J. Sel. Topics Appl. Earth Observ. Remote Sens.*, vol. 7, no. 12, pp. 4937–4938, Dec. 2014.

[14] V. C. Chen, F. Li, S. Ho, and H. Wechsler, "Micro-Doppler effect in radar-phenomenon, model, and simulation study," *IEEE Trans. Aerosp. Electron. Syst.*, vol. 24, no. 6, pp. 1–21, Jun. 2006.

[15] V. C. Chen, "Doppler signatures of radar backscattering from objects with micro-motions," *IET Signal Process.*, vol. 2, no. 3, pp. 291–300, Sep. 2008.

[16] X. Pan, W. Wang, J. Liu, L. Ma, D. Feng, and G. Wang, "Modulation effect and ISAR imaging of rotationally symmetric ballistic targets with precession," *IET Radar, Sonar, Navigat.*, vol. 9, no. 7, pp. 950–958, 2013.

[17] T. Thayaparan, L. J. Stanković, M. Daković, and V. Popović, "Micro-Doppler parameter estimation from a fraction of the period," *IET Signal Process.*, vol. 4, pp. 201–212, Jun. 2010.

[18] X. Pan, W. Wang, J. Liu, D.-J. Feng, Y. Liu, and G. Wang, "Features extraction of rotationally symmetric ballistic targets based on micro-Doppler," *Progr. Electromagn. Res.*, vol. 137, pp. 727–740, Mar. 2013.

[19] K. T. Kim, "Focusing of high range resolution profiles of moving targets using stepped frequency waveforms," *IET Radar, Sonar, Navigat.*, vol. 4, no. 4, pp. 564–575, 2010.

[20] F. Zhu, Q. Zhang, Q. Lei, and Y. Luo, "Reconstruction of moving target's HRRP using sparse frequency-stepped chirp signal," *IEEE Sensors J.*, vol. 11, no. 10, pp. 2327–2334, Oct. 2011.

[21] Q. Zhang, T. S. Yeo, H. S. Tan, and Y. Luo, "Imaging of a moving target with rotating parts based on the Hough transform," *IEEE Trans. Geosci. Remote Sens.*, vol. 46, no. 1, pp. 291–299, Jan. 2008.

[22] X. Wu, X. Wang, and H. Lu, "Motion feature extraction for stepped frequency radar based on Hough transform," *IET Radar, Sonar, Navigat.*, vol. 4, no. 1, pp. 17–27, 2010.

[23] K. Li, X. Liang, Q. Zhang, Y. Luo, and H. Li, "Micro-Doppler signature extraction and ISAR imaging for target with micromotion dynamics," *IEEE Trans. Geosci. Remote Sens.*, vol. 8, no. 3, pp. 411–415, Mar. 2011.

[24] V. C. Chen and H. Ling, *Time-Frequency Transforms for Radar Imaging and Signal Analysis*. Boston, MA, USA: Artech House, 2001.

[25] L. Du, H. Liu, Z. Bao, and J. Zhang, "A two-distribution compounded statistical model for radar HRRP target recognition," *IEEE Trans. Signal Process.*, vol. 54, no. 6, pp. 2226–2238, Jun. 2006.

[26] Y. Luo, Q. Zhang, C.-W. Qiu, X.-J. Liang, and K.-M. Li, "Micro-Doppler effect analysis and feature extraction in ISAR imaging with stepped-frequency chirp signals," *IEEE Trans. Geosci. Remote Sens.*, vol. 48, no. 4, pp. 2087–2098, Apr. 2010.

[27] V. C. Chen, *The Micro-Doppler Effect in Radar*. Boston, MA, USA: Artech House, 2011.

[28] C. Özdemir, *Inverse Synthetic Aperture Radar Imaging With MATLAB Algorithms*. Mersin, Turkey: Wiley, 2011.

[29] V. C. Chen and M. Martorella, *Inverse Synthetic Aperture Radar Imaging: Principles, Algorithms and Applications*, Edison, NJ, USA: SciTech Publishing, 2014.

[30] W. Zhang, G. Xu, and Y. Wang, "Pitch estimation based on circular AMDF," in *Proc. IEEE Int. Conf. Acoust., Speech, Signal Process. (ICASSP)*, vol. 1. May 2002, pp. I-341–I-344.
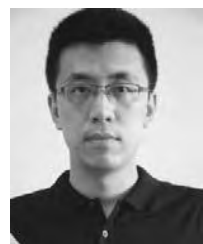
XIAO-YI PAN was born in Anhui, China, in 1986. He received the M.S. degree and the Ph.D. degree in information and communication engineering from the National University of Defense Technology, Changsha, China, in 2009 and 2014, respectively.

He is currently a Lecturer with the National University of Defense Technology. His fields of interest include inverse synthetic aperture radar imaging, feature extraction, and electromagnetic environment effects.

JIAQI LIU was born in Hunan, China, in 1963. In 2007, he received the Ph.D. degree in circuit and systems from Beihang University, Beijing, China.

He currently serves as the Vice Director and a Leading Research Fellow of National Key Laboratory of Science and Technology on Test Physics and Numerical Mathematics. His research area is signal processing and target recognition.

LE-TAO XU was born in Shandong, China, in 1987. He received the B.S. degree from the University of Electronic Science and Technology of China, Chengdu, China, in 2010, and the M.S. degree from the National University of Defense Technology, Changsha, China, in 2012, where he is currently pursuing the Ph.D. degree.

His research interests include inverse synthetic aperture radar imaging and electromagnetic environment effects.

XIA AI was born in Yulin, Shaanxi, China, in 1986. He received the Ph.D. degree in electromagnetics and microwave technology from Xidian University, Xi'an, China, in 2013.

He currently serves as a Senior Engineer of the National Key Laboratory of Science and Technology on Test Physics and Numerical Mathematics. His research interests include computational electromagnetics, radar target recognition, and electromagnetic scattering characteristic of complex.
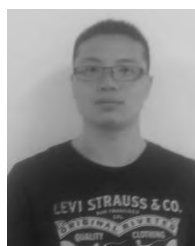
QIANPENG XIE was born in Henan, China, in 1991. He received the B.S. and M.S. degrees from the Electronic Engineering Institute, Hefei, China, in 2014 and 2016, respectively.

He is currently pursuing the Ph.D. degree in the National University of Defense Technology. His research interests include cognitive radar, radar signal processing, and electromagnetic environment effects.

BO YU received the M.S. and Ph.D. degrees from the National University of Defense Technology in 2009 and 2013, respectively.

He is currently a Researcher with the National University of Defense Technology. His research interest includes computer network and information security.

CHENG LI was born in Hubei, China, in 1985. He received the M.S. and Ph.D. degrees in information and communication engineering from the National University of Defense Technology, Changsha, China, in 2009 and 2015, respectively.

He is currently an Engineer of the Nanjing Telecommunication Technology Research Institute. His fields of interest include signal processing, pattern recognition, and wireless communication.

● ● ●